Eur. Phys. J. C (2009) 64: 627–636
DOI 10.1140/epjc/s10052-009-1177-x

THE EUROPEAN
PHYSICAL JOURNAL C

Regular Article - Experimental Physics

Precise measurement of $\Gamma(K \to e\nu(\gamma))/\Gamma(K \to \mu\nu(\gamma))$ and study of $K \to e\nu\gamma$

The KLOE Collaboration

F. Ambrosino[3,4], **A. Antonelli**[1], **M. Antonelli**[1,a], **F. Archilli**[8,9], **P. Beltrame**[2], **G. Bencivenni**[1], **C. Bini**[6,7], **C. Bloise**[1], **S. Bocchetta**[10,11], **F. Bossi**[1], **P. Branchini**[11], **G. Capon**[1], **D. Capriotti**[10], **T. Capussela**[1], **F. Ceradini**[10,11], **P. Ciambrone**[1], **E. De Lucia**[1], **A. De Santis**[6,7], **P. De Simone**[1], **G. De Zorzi**[6,7], **A. Denig**[2], **A. Di Domenico**[6,7], **C. Di Donato**[4], **B. Di Micco**[10,11], **M. Dreucci**[1], **G. Felici**[1], **S. Fiore**[6,7], **P. Franzini**[6,7], **C. Gatti**[1], **P. Gauzzi**[6,7], **S. Giovannella**[1], **E. Graziani**[11], **M. Jacewicz**[1], **V. Kulikov**[13], **G. Lanfranchi**[1], **J. Lee-Franzini**[1,12], **M. Martini**[1,5], **P. Massarotti**[3,4], **S. Meola**[3,4], **S. Miscetti**[1], **M. Moulson**[1], **S. Müller**[2], **F. Murtas**[1], **M. Napolitano**[3,4], **F. Nguyen**[10,11], **M. Palutan**[1], **A. Passeri**[11], **V. Patera**[1,5], **P. Santangelo**[1], **B. Sciascia**[1], **A. Sibidanov**[1], **T. Spadaro**[1,b], **L. Tortora**[11], **P. Valente**[7], **G. Venanzoni**[1], **R. Versaci**[1,5]

[1] Laboratori Nazionali di Frascati dell'INFN, Frascati, Italy
[2] Institut für Kernphysik, Johannes Gutenberg-Universität, Mainz, Germany
[3] Dipartimento di Scienze Fisiche dell'Università "Federico II", Napoli, Italy
[4] INFN Sezione di Napoli, Napoli, Italy
[5] Dipartimento di Energetica dell'Università "La Sapienza", Rome, Italy
[6] Dipartimento di Fisica dell'Università "La Sapienza", Rome, Italy
[7] INFN Sezione di Roma, Rome, Italy
[8] Dipartimento di Fisica dell'Università "Tor Vergata", Rome, Italy
[9] INFN Sezione di Roma Tor Vergata, Rome, Italy
[10] Dipartimento di Fisica dell'Università "Roma Tre", Rome, Italy
[11] INFN Sezione di Roma Tre, Rome, Italy
[12] Physics Department, State University of New York, Stony Brook, USA
[13] Institute for Theoretical and Experimental Physics, Moscow, Russia

Received: 21 July 2009 / Revised: 14 September 2009 / Published online: 28 October 2009

Abstract We present a precise measurement of the ratio $R_K = \Gamma(K \to e\nu(\gamma))/\Gamma(K \to \mu\nu(\gamma))$ and a study of the radiative process $K \to e\nu\gamma$, performed with the KLOE detector. The results are based on data collected at the Frascati e^+e^- collider DAΦNE for an integrated luminosity of 2.2 fb^{-1}. We find $R_K = (2.493 \pm 0.025_{\text{stat}} \pm 0.019_{\text{syst}}) \times 10^{-5}$, in agreement with the Standard Model expectation. This result is used to improve constraints on parameters of the Minimal Supersymmetric Standard Model with lepton flavor violation. We also measured the differential decay rate $d\Gamma(K \to e\nu\gamma)/dE_\gamma$ for photon energies $10 < E_\gamma < 250$ MeV. Results are compared with predictions from theory.

PACS 13.20.Eb

1 Introduction

The decay $K^\pm \to e^\pm\nu$ is strongly suppressed, $\sim$few$\times 10^{-5}$, because of conservation of angular momentum and the vector structure of the charged weak current. It therefore offers the possibility of detecting minute contributions from physics beyond the Standard Model (SM). This is particularly true of the ratio $R_K = \Gamma(K \to e\nu)/\Gamma(K \to \mu\nu)$ which, in the SM, is calculable without hadronic uncertainties [1–3]. Physics beyond the SM, for example multi-Higgs effects inducing an effective pseudo-scalar interaction, can change the value of R_K. It has been shown in [4] that deviations of R_K of up to *a few percent* are possible in minimal supersymmetric extensions of the SM (MSSM) with non vanishing e-τ scalar lepton mixing. To obtain accurate predictions, the radiative process $K \to e\nu\gamma$ ($K_{e2\gamma}$) must be included. In $K_{e2\gamma}$, photons can be produced via internal-bremsstrahlung (IB) or direct-emission (DE), the latter being dependent on the hadronic structure. Interference among the two processes is negligible [5]. The DE contribution to

---

[a] e-mail: Mario.Antonelli@lnf.infn.it
[b] e-mail: Tommaso.Spadaro@lnf.infn.it

the total width is approximately equal to that of IB [5] but is presently known with a 15% fractional accuracy [6].

R_K is *defined* to be inclusive of IB, ignoring however DE contributions. A recent calculation [3], which includes order $e^2 p^4$ corrections in chiral perturbation theory (χPT), gives:

$$R_K = (2.477 \pm 0.001) \times 10^{-5}. \tag{1}$$

R_K is not directly measurable, since IB cannot be distinguished from DE on an event-by-event basis. Therefore, in order to compare data with the SM prediction at the percent level or better, the DE contribution must be carefully estimated and subtracted.[1]

DE can proceed through vector and axial-vector transitions, with effective coupling V and A, respectively:

$$\begin{aligned}\frac{d^2\Gamma(K_{e2\gamma},\mathrm{DE})}{dx\,dy} &= \frac{G_F^2|\sin\theta_\mathrm{C}|^2\alpha_\mathrm{em}M_K^5}{64\pi^2} \\ &\quad\times\left[(V+A)^2 f_{\mathrm{DE}^+}(x,y) + (V-A)^2 f_{\mathrm{DE}^-}(x,y)\right],\end{aligned} \tag{2}$$

where G_F is the Fermi coupling, θ_C is the Cabibbo angle [7], $x = 2E_\gamma/M_K$, $y = 2E_e/M_K$ are the dimensionless photon and electron energies in the kaon rest frame (both lying between 0 and 1), and

$$\begin{aligned} f_{\mathrm{DE}^+}(x,y) &= (x+y-1)^2(1-x), \\ f_{\mathrm{DE}^-}(x,y) &= (1-y)^2(1-x). \end{aligned} \tag{3}$$

Terms proportional to $(m_e/M_K)^2$ are neglected. The photon energy spectrum in the CM is shown in Fig. 1 with its IB, DE$^+$, and DE$^-$ contributions.[2] The DE terms are evaluated with constant V, A coupling and calculated in χPT at $\mathcal{O}(p^4)$ [5].

We define the rate R_{10} as:

$$R_{10} = \Gamma(K \to e\nu(\gamma),\ E_\gamma < 10\,\mathrm{MeV})/\,\Gamma(K \to \mu\nu). \tag{4}$$

Evaluating the IB spectrum to $\mathcal{O}(\alpha_\mathrm{em})$ with resummation of leading logarithms, R_{10} includes $93.57 \pm 0.07\%$ of the IB,

$$R_{10} = R_K \times (0.9357 \pm 0.0007). \tag{5}$$

The DE contribution in this range is expected to be negligible. However, the event sample used to measure R_{10} (see Sect. 3) still contains a small DE contribution, in particular for decays with high electron momentum in the CM, p_e. In order to subtract this contribution, we have also measured the differential width

$$\frac{dR_\gamma}{dE_\gamma} = \frac{1}{\Gamma(K \to \mu\nu)}\frac{d\Gamma(K \to e\nu\gamma)}{dE_\gamma}, \tag{6}$$

for $E_\gamma > 10$ MeV and $p_e > 200$ MeV requiring photon detection, both to test χPT predictions for the DE terms and to reduce possible systematic uncertainties on the R_{10} measurement.

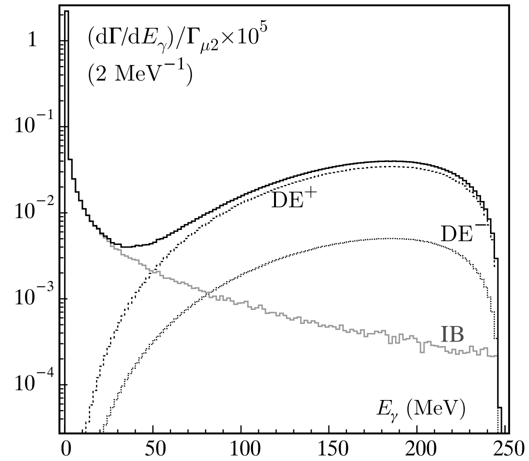

Fig. 1 CM photon spectrum for $K_{e2\gamma}$ decay. Inner bremsstrahlung (IB) and positive and negative helicity direct emission (DE$^+$ and DE$^-$) contributions are also shown

2 DAΦNE and KLOE

DAΦNE, the Frascati ϕ factory, is an e^+e^- collider operated at a total energy $\sqrt{s} = m_\phi \sim 1.02$ GeV. ϕ mesons are produced, essentially at rest, with a visible cross section of ∼3.1 μb and decay into K^+K^- pairs with a BR of ∼49%. During 2001–2005 KLOE collected an integrated luminosity of about 2.2 fb^{-1}, corresponding to ∼3.3 billion of K^+K^- pairs. Kaon production and decay are studied with the KLOE detector, consisting essentially of a drift chamber, DC, surrounded by an electromagnetic calorimeter, EMC. A superconducting coil provides a 0.52 T magnetic field parallel to the cylinder axis. After entering the DC, kaons have a momentum of ∼100 MeV corresponding to a velocity $\beta_K \sim 0.2$. The mean kaon path is $\lambda_K \sim 90$ cm.

The DC, see [8], is a cylinder of 4 m in diameter and 3.3 m in length. It has 12,582 tungsten sense wires and 37,746 aluminum field wires arranged in 58 stereo layers uniformly filling the sensitive volume. The chamber shell is made of carbon-fiber epoxy composite and the gas used is a 90% helium, 10% isobutane mixture. These features maximize transparency to photons and reduce multiple scattering; the effective radiation length of the gas-wires composite

---

[1] The same arguments apply in principle to $\Gamma(K \to \mu\nu)$. However, there is no helicity suppression in this case. IB must be included and DE can be safely neglected.

[2] "+" and "−" refer to the photon helicity.

is ∼900 m. The DC position resolutions are $\sigma_{xy} \approx 150$ μm and $\sigma_z \approx 2$ mm. The momentum resolution for tracks at large polar angle is $\sigma(p_\perp/p_\perp) \leq 0.4\%$.

The EMC, see [9], is a lead scintillating-fiber sampling calorimeter consisting of a barrel and two endcaps and covers 98% of the solid angle. The EMC modules are read out at both ends by photomultiplier tubes. The calorimeter structure has an X_0 of ∼1.5 cm and the readout granularity is $\sim 4.4 \times 4.4$ cm^2, with five layers in depth. The energy and time resolutions are $\sigma_E/E \sim 5.7\%/\sqrt{E(\mathrm{GeV})}$ and $\sigma_T = 54\ \mathrm{ps}/\sqrt{E(\mathrm{GeV})} \oplus 140$ ps, respectively. The EMC provides also particle identification, based on the pattern of energy deposits in the EMC cells. An example of the difference between electron and muon patterns is shown in Fig. 2.

The trigger [10] uses both EMC and DC information. Two energy deposits above threshold ($E > 50$ for barrel and > 150 MeV for endcaps) are required for the EMC trigger. The DC trigger is based on wire hit multiplicity. The logical OR of EMC and DC triggers is used for the measurement presented. The trigger efficiency is evaluated from data.

Cosmic-ray rejection is performed by the trigger hardware. Residual cosmic ray and machine background events are removed by an offline software filter using calorimeter information before track reconstruction.

The detector response is obtained by means of the KLOE Monte Carlo (MC) simulation program Geanfi, [11]. Changes in machine parameters and background conditions are simulated on a run-by-run basis in order to properly take into account the induced effects.

The MC samples used for this analysis correspond to integrated luminosities of 4.4 fb^{-1} for the main $K^\pm$ decay modes and of 500 fb^{-1} for decays with BR's less than 10^{-4}. The effects of initial- and final-state radiation are included in the simulation at the event generator level [11, 12]. For $K_{e2\gamma}$ events, the IB component is described at $\mathcal{O}(e^2)$ including resummation of leading logarithms [12], while the DE component is described with χPT at $\mathcal{O}(e^2 p^4)$ [5]. Unless otherwise specified, when comparing data with simulation we rescale MC samples to an integrated luminosity of 2.2 fb^{-1}, assume the SM value for R_K, and use the theoretical prediction for the DE/IB fraction.

3 Selection of leptonic kaon decays

$K^\pm$ decays are signaled by the observation of two tracks with the following conditions. One track must originate at the interaction point (IP) and have momentum in the interval {70, 130} MeV, consistent with being a kaon from ϕ-decay. The second track must originate at the end of the previous track and have momentum larger than that of the kaon, with the same charge. The second track is taken as a decay product of the kaon. The point of closest approach of the two tracks is taken as the kaon decay point D and must satisfy $40 < r_\mathrm{D} < 150$ cm, $|z_\mathrm{D}| < 80$ cm. The geometrical acceptance with these conditions is ∼56%, while the decay point reconstruction efficiency is ∼51%. The above search is applied for each kaon charge separately. From the measured kaon and decay particle momenta, $\mathbf{p}_K$ and $\mathbf{p}_\mathrm{d}$, we compute the squared mass m_ℓ^2 of the lepton for the decay $K \to \ell\nu$ assuming zero missing mass:

$$m_\ell^2 = (E_K - |\mathbf{p}_K - \mathbf{p}_\mathrm{d}|)^2 - \mathbf{p}_\mathrm{d}^2. \tag{7}$$

The distribution of m_ℓ^2 is shown in Fig. 3, upper curve, from MC simulation. The muon peak is quite evident, higher masses corresponding to non leptonic and semileptonic decays. No signal from $K \to e\nu$ (K_{e2}) decay is visible. The very large background around zero mass is the tail of the $K \to \mu\nu$ ($K_{\mu2}$) peak, due to poor measurements of p_K, p_d or the decay angle, $\alpha_{K\mathrm{d}}$. The expected signal from $K_{e2\gamma}$ is also shown in Fig. 3, lower curves, separately for $E_\gamma > 10$ and < 10 MeV. The expected number of K_{e2} decays in the sample is ∼30,000. A background rejection of at least

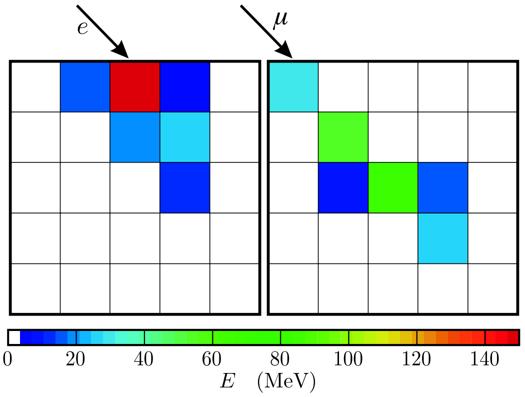

Fig. 2 Energy deposit pattern in the EMC cells for a 200 MeV electron (*left*) and a muon (*right*) from two $K_L \to \pi\ell\nu$ events

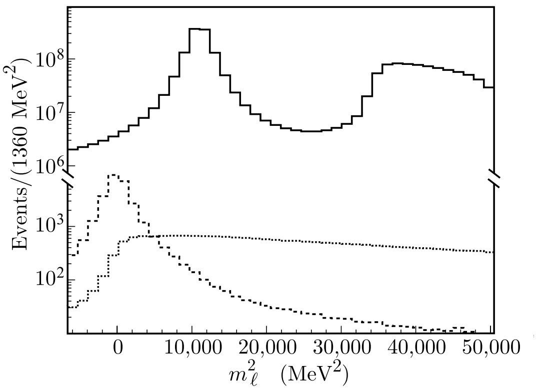

Fig. 3 MC distribution of m_ℓ^2, *solid line*. The contribution of $K_{e2\gamma}$ with $E_\gamma < 10$ MeV (>10 MeV) is shown by the *dashed* (*dotted*) *lines*

1000 is necessary, to obtain a 1% precision measurement of $\Gamma(K_{e2})$, with an efficiency of ∼30%.

The kinematics of the two-body decay $\phi \to K^+K^-$ provides an additional measurement of p_K. The kaon momentum at the IP is computed from its direction at the IP and the known value of the ϕ 4-momentum.[3] The computed value is extrapolated to the decay point D, accounting for K energy losses in the material traversed. These are relevant, since the kaon velocity is ∼0.2. The material amount traversed has been determined to within 1%, thus reducing its contribution to the momentum resolution to below 0.5 MeV. The total resolution of the measurement is ∼1 MeV, comparable with that from track reconstruction. We require the two p_K determinations to agree within 5 MeV.

Further cuts are applied to the daughter track. The resolution of track parameters is improved by rejecting badly reconstructed tracks, i.e., with $\chi^2(\text{track fit})/\text{ndf} > 7.5$. Events with poorly determined decay angles are mostly due to tracks with improper left-right assignment in the reconstruction of the DC hits. This happens often when a large majority of the hits associated to the daughter track are on a single stereo view. These events are removed by a cut on the fractional difference of the number of hits on each stereo view.

Finally, using the expected errors on p_K and p_d from tracking, we compute event by event the error on m_ℓ^2, δm_ℓ^2. The distribution of δm_ℓ^2 depends slightly on the decay angle $\alpha_{K\text{d}}$, which in turn has different distribution for K_{e2} and $K_{\mu 2}$. Events with large value of δm_ℓ^2 are rejected: $\delta m_\ell^2 < \delta_\text{max}$, with δ_max defined as a function of $\alpha_{K\text{d}}$, to equalize the losses due to this cut for K_{e2} and $K_{\mu 2}$.

The effect of the quality cuts on the m_ℓ^2 resolution is shown in Fig. 4. The background in the K_{e2} signal region is effectively reduced by more than one order of magnitude with an efficiency of ∼70% for both K_{e2} and $K_{\mu 2}$.

Information from the EMC is also used to improve background rejection. To this purpose, we extrapolate the secondary track to the EMC surface and associate it to a nearby EMC cluster. This requirement produces a signal loss of about 8%.

Energy distribution and position along the shower axis of all cells associated to the cluster allow for e/μ particle identification. For electrons, the cluster energy E_cl is a measurement of the particle momentum p_d, so that E_cl/p_d peaks around 1, while for muons E_cl/p_d is on average smaller than 1. Moreover, electron clusters can also be distinguished from μ (or π) clusters by exploiting the longitudinal segmentation of the EMC: electrons shower and deposit their energy mainly in the first plane of EMC, while muons behave like minimum ionizing particles in the first plane and deposit a sizeable fraction of their kinetic energy from the third plane onward, when they are slowed down to rest (Bragg's peak), see Fig. 2.

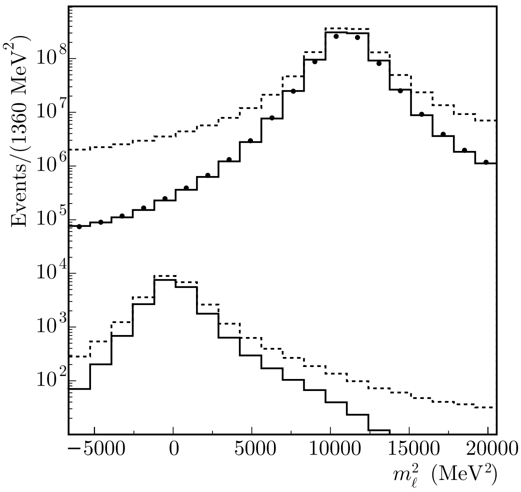

Fig. 4 m_ℓ^2 spectrum before (*dashed*) and after (*solid*) quality cuts for MC $K_{\mu 2}$ (*upper plots*) and K_{e2} with $E_\gamma < 10$ MeV (*lower plots*). *Black dots* represent data after quality cuts

All useful information about shower profile and total energy deposition are combined with a 12-25-20-1 structure neural network trained on $K_L \to \pi\ell\nu$ and $K_{\mu 2}$ data, taking into account variations of the EMC response with momentum and impact angle on the calorimeter. The distribution of the neural network output, *NN*, for a sample of $K_L \to \pi e \nu$ events is shown in Fig. 5, for data and MC. Additional separation has been obtained using time of flight information. The data distribution of *NN* as function of m_ℓ^2 is shown in Fig. 6. A clear $K \to e\nu$ signal can be seen at $m_\ell^2 \sim 0$ and $NN \sim 1$.

Some 32% of the events with a K decay in the fiducial volume have a reconstructed kink matching the required quality criteria *and* an EMC cluster associated to the lepton track; this holds for both K_{e2} and $K_{\mu 2}$. In the selected sample, the contamination from K decays other than $K_{\ell 2}$ is negligible, as evaluated from MC. R_{10}, (4), is obtained without requiring the presence of the radiated photon. The number of $K \to e\nu(\gamma)$ events is determined with a binned likelihood fit to the two-dimensional *NN* vs. m_ℓ^2 distribution. Distribution shapes for signal and $K_{\mu 2}$ background are taken from MC; the normalization factors for the two components are the only fit parameters. The fit has been performed in the region $-3700 < m_\ell^2 < 6100$ MeV^2 and $NN > 0.86$. The fit region accepts ∼90% of $K \to e\nu(\gamma)$ events with $E_\gamma < 10$ MeV, as evaluated from MC. A small fraction of fitted $K \to e\nu(\gamma)$ events have $E_\gamma > 10$ MeV: the value of this "contamination", f_DE, is fixed in the fit to the expectation from simulation, $f_\text{DE} = 10.2\%$. A systematic error related to this assumption is discussed in Sect. 5.

---

[3] The average value of the ϕ 4-momentum is determined on a run-by-run basis from Bhabha events, while event-by-event fluctuations are dominated by the beam energy spread.

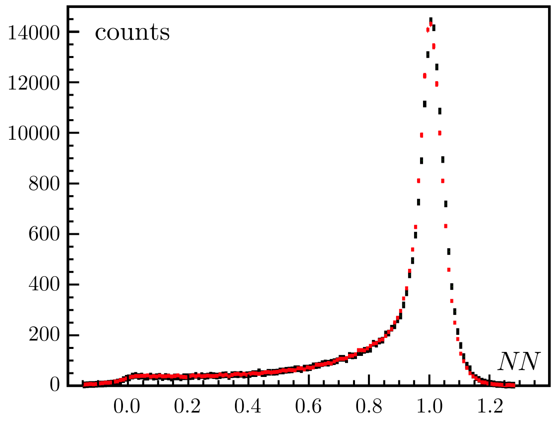

Fig. 5 (Color online) Neural-network output, NN, for electrons of a $K_L \to \pi e \nu$ sample from data (*black*) and MC (*red*)

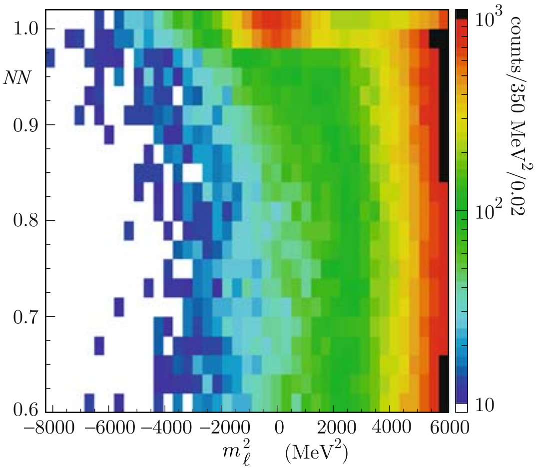

Fig. 6 Data density in the NN, m_ℓ^2 plane

We count $7064 \pm 102 K^+ \to e^+\nu(\gamma)$ events and $6750 \pm 101 K^- \to e^-\bar{\nu}(\gamma)$, 89.8% of which have $E_\gamma < 10$ MeV. The signal-to-background correlation is ∼20% and the χ^2/ndf is 113/112 for K^+ and 140/112 for K^-.[4] Figure 7 shows the sum of fit results for K^+ and K^- projected onto the m_ℓ^2 axis in a signal ($NN > 0.98$) and a background ($NN < 0.98$) region. The residual contribution of $K_{e2\gamma}$ events with $E_\gamma > 10$ MeV is also shown.

The number of $K_{\mu2}$ events is obtained from a fit to the m_ℓ^2 distribution after quality cuts are applied, see Fig. 4. The fraction of background events under the muon peak is estimated from MC to be less than one per mil. We count 2.878×10^8 (2.742×10^8) $K^+ \to \mu^+\nu(\gamma)$ ($K^- \to \mu^-\bar{\nu}(\gamma)$) events. The difference between K^+ and K^- counts is due to the higher K^- nuclear-interaction cross section in the material traversed.

3.1 $K_{e2\gamma}$ event counting

In order to study $K_{e2\gamma}$ decays, we apply the same selection criteria as for K_{e2}, but a tighter PID cut, $NN > 0.98$. We also require one and only one photon in time with the K decay. Photons are identified by selecting a cluster with energy greater than 20 MeV. This requirement reduces machine background and suppresses most of the IB events, leaving a sample dominated by direct emission process (DE). Moreover, the difference between the photon and the electron measured time of flight has to lie within two standard deviations from its expected value. The fraction of signal events satisfying all of these additional requests is ∼25%. The m_ℓ^2 distribution for the selected events, again evaluated from (7), is shown in Fig. 8 for data and MC. $K_{e2\gamma}$ decays with $p_e > 200$ MeV and $p_e < 200$ MeV are shown separately. The high-momentum component is dominated by the DE$^+$ process, DE$^-$ accounting for 2% only (2), and is the only relevant for the evaluation of the systematic uncertainty affecting the R_{10} measurement: high p_e values correspond to low values of m_ℓ^2 where the K_{e2} signal lies. The low-momentum component, with contributions from both DE$^+$ and DE$^-$ processes, is completely overwhelmed by K_{e3} events with one undetected photon from π^0 decay.

Further rejection of K_{e3} events is provided by kinematics. The photon energy in the laboratory frame, $E_\gamma(\text{lab})$, can be calculated for $K_{e2\gamma}$ decays from the measured photon direction, the kaon momentum p_K and the electron momentum p_e, with a resolution of ∼12 MeV. The resolution on $\Delta E = E_\gamma(\text{lab}) - E_{\gamma,\,\text{EMC}}$ is that of the calorimeter, $\sigma \sim 30$ MeV for $E_\gamma(\text{lab}) = 200$ MeV. The number of $K_{e2\gamma}$ events is found from a binned likelihood fit in the $\Delta E/\sigma$-m_ℓ^2 plane. This provides a better signal to noise figure, compared to using cuts on ΔE and m_ℓ^2. Distribution shapes for signal and $K_{\mu2}$ and K_{e3} backgrounds are taken from MC. The amounts of the three components are the fit parameters.

For the measurement of the differential width, (6), we boost $E_\gamma(\text{lab})$ to the kaon rest frame (E_γ) and perform independent fits for five E_γ bins between 10 MeV and the kinematic limit, as defined in Table 1. For each E_γ bin, we are able to extract the number of $K_{e2\gamma}$ events with $p_e > 200$ MeV. Because of limited statistics, the counting is done combining the kaon charges. Results are listed in Table 1. The total $K_{e2\gamma}$ count, with $E_\gamma > 10$ MeV and $p_e > 200$ MeV, is 1484 ± 63 events. Figure 9 shows the sum of the fit results on all of the E_γ bins, projected onto the $\Delta E/\sigma$ axis for the signal region (top), defined as $m_\ell^2 < 8000$ MeV^2 or $14000 < m_\ell^2 < 20000$ MeV^2, and for the background region (bottom). In the latter, $K_{\mu2}$ dominate the region $8000 < m_\ell^2 < 14000$ MeV^2, while K_{e3} dominate the region above 20000 MeV^2 (see Fig. 8).

---

[4] The χ^2/ndf of the K^- fit improves to 114/98 for a fit range $NN > 0.88$, with negligible difference in the measured value for R_{10}.

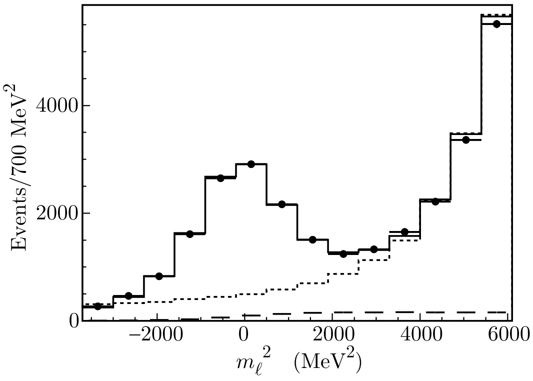

Fig. 7 Fit projections onto the m_ℓ^2 axis for $NN > 0.98$ (*left*) and $NN < 0.98$ (*right*), for data (*black dots*), MC fit (*solid line*), and $K_{\mu2}$ background (*dotted line*). The contribution from K_{e2} events with $E_\gamma > 10$ MeV is visible in the *left panel* (*dashed line*)

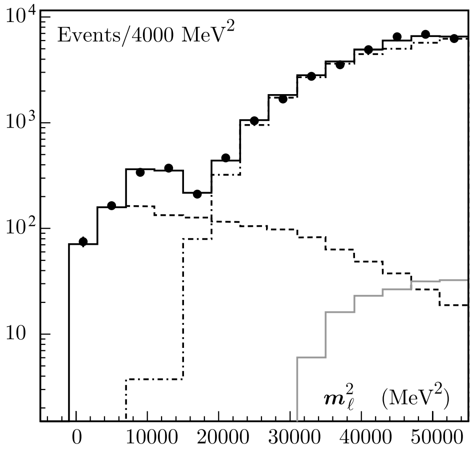

Fig. 8 m_ℓ^2 distribution for data (*black dots*) and MC (*solid line*) for events with a detected photon. MC $K_{e2\gamma}$ events with $p_e < 200$ MeV (*gray*), $p_e > 200$ MeV (*dashed*) and K_{e3} events (*dot-dashed*) are shown separately

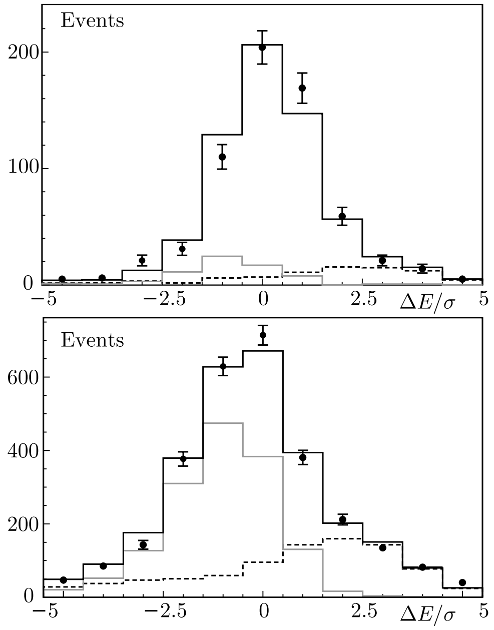

Fig. 9 $K_{e2\gamma}$ fit projections onto the $\Delta E/\sigma(\Delta E)$ axis for the signal region (as defined in the text, *top*) and background region (*bottom*) for data (*black dots*), MC fit (*solid line*), $K_{\mu2}$ (*dashed line*) and K_{e3} (*gray line*). All E_γ bins are added

4 Efficiency

The ratios of K_{e2} to $K_{\mu2}$ and $K_{e2\gamma}$ to $K_{\mu2}$ efficiencies are evaluated with MC and corrected for possible differences between data and MC, using control samples. We evaluate data-MC corrections separately for each of the following analysis steps: decay point reconstruction (kink), quality cuts, cluster-charged particle association; for $K_{e2\gamma}$ events, the efficiency for selection of a photon cluster is added, too. For each step, the correction is defined as the ratio of data and MC efficiencies measured on the control sample, each folded with the proper kinematic spectrum of K_{e2} (or $K_{\mu2}$) events.

Decay point reconstruction efficiencies are evaluated using pure samples of $K_{\mu2}$ and K_{e3}; these are tagged by the identification of the two-body decay, $K_{\mu2}$ or $K \to \pi\pi^0$ ($K_{\pi2}$), of the other kaon [13] and selected with tagging and EMC information only, without using tracking.

Table 1 Fit results for the number of $K_{e2\gamma}$ events with $p_e > 200$ MeV, in five E_γ energy bins

E_γ (MeV)	10 to 50	50 to 100	100 to 150	150 to 200	200 to 250
Signal counts	55 ± 16	219 ± 24	463 ± 32	494 ± 38	253 ± 26
χ^2/ndf	80/66	141/105	87/106	100/106	116/102

A 99.5% pure $K^{\pm}_{\mu 2}$ sample is obtained with $K^{\mp}$ tagging plus one and only one EMC cluster with energy $E >$ 90 MeV, *not due* to the tagging kaon decay products. The properties of the selected $K_{\mu 2}$ event are evaluated using time and position of the cluster and the kaon momentum obtained from the tagging (with 1% resolution). The muon momentum and the decay point position are determined a priori, without using the kaon and electron tracks, with a resolution of about 5 MeV and about 2 cm, respectively. The tracking efficiency is determined as a function of the decay point position and the decay angle, by counting the number of events in which a kink is reconstructed out of the number of $K_{\mu 2}$ candidate events.

$K^{\pm}_{e3}$ decays are selected in $K^{\mp}$ tagged events first detecting the photons from π^0 decay with time of flights consistent with a single point in the tagged kaon track obtained from the tagging kaon. Second, a third cluster with energy, time, and position consistent with the expectation from a K_{e3} decay is selected. The electron momentum and the kaon decay point are determined a priori with a resolution of ∼20 MeV (dominated by the measurement of π^0 momentum) and ∼2 cm, respectively.

The corrections to MC efficiencies range between 0.90 and 0.99 depending on the decay point position and on the decay angle. The simulation is less accurate in case of overlap between lepton and kaon tracks, and with decays occurring close to the inner border of the fiducial volume.

Samples of $K_L(e3)$, $K_L(\mu 3)$, and $K_{\mu 2}$ decays with a purity of 99.5%, 95.4%, and 100.0% respectively, are used to evaluate lepton cluster efficiencies. These samples are selected using tagging and DC information only, without using calorimeter, see [14–16]. The efficiency has been evaluated as a function of the particle momentum separately for barrel and endcap. The correction to MC efficiencies ranges between 0.98 and 1.01 depending on the momentum and on the point of impact on the calorimeter.

The single-photon detection efficiency for data and MC is evaluated as a function of photon energy using $K_{\pi 2}$ events, in which one of the two photons from π^0 decay is identified, allowing an a priori determination of the position and of the energy of the second one. The average correction factor to MC efficiency is ∼0.98.

The trigger efficiency has been evaluated solely from data. The probabilities $\epsilon^{\text{TRG}}_{\text{EMC}}$ ($\epsilon^{\text{TRG}}_{\text{DC}}$) for the EMC (DC) trigger condition to be satisfied in a DC-triggered (EMC-triggered) event are evaluated in K_{e2}-enriched and $K_{\mu 2}$-pure samples. The efficiency for the logical OR of the EMC and DC trigger conditions is given by $\epsilon^{\text{TRG}}_{\text{EMC}} + \epsilon^{\text{TRG}}_{\text{DC}} - \epsilon^{\text{TRG}}_{\text{EMC}} \times \epsilon^{\text{TRG}}_{\text{DC}}$, and it is ∼0.99 for both K_{e2} and $K_{\mu 2}$, with a ratio $\epsilon^{\text{TRG}}(K_{e2})/\epsilon^{\text{TRG}}(K_{\mu 2}) = 0.9988(5)$. A possible bias on the previous result due to correlation between EMC and DC triggers is also taken into account, which is evaluated to be 0.997(1) using MC simulation.

The event losses induced by the cosmic veto applied at the trigger level and by the background rejection filter applied offline (FILFO) are evaluated from samples of downscaled events, in which the veto conditions are registered but not enforced. The ratio of K_{e2} to $K_{\mu 2}$ efficiencies are 1.0013(2) and 0.999(4) for cosmic veto and FILFO, respectively. The statistical error due to the FILFO correction is 0.4%, and dominates the total uncertainty in trigger, cosmic veto, and FILFO corrections.

5 Systematic errors

The absolute values of all of the systematic uncertainties on R_{10} and R_γ, the integral of (6) for $E_\gamma > 10$ MeV, are listed in Table 2; the statistical uncertainties, 1% and 4.5% fractional respectively, are reported for comparison. All of the sources of systematic error are discussed below.

To minimize possible biases on K_{e2} event counting due to the limited knowledge of the momentum resolution, we used $K_{\mu 2}$ data to carefully tune the MC response on the tails of the m^2_ℓ distribution. This has been performed in sidebands of the *NN* variable, to avoid bias due to the presence of the K_{e2} signal. Similarly, for the *NN* distribution the EMC response in the MC has been tuned at the level of single cell, using $K_{\ell 3}$ data control samples. Residual differences between data and MC K_{e2} and $K_{\mu 2}$ *NN* shapes have been corrected by using the same control samples. Finally, to evaluate the systematic error associated with these procedures, we studied the variation of the results with different choices of fit range, corresponding to a change of overall purity from ∼75% to ∼10%, for $K \to e\nu(\gamma)$ with $E_\gamma < 10$ MeV, and from ∼31% to ∼10%, for $K \to e\nu(\gamma)$ with $E_\gamma > 10$ MeV and $p_e > 200$ MeV. The results are stable within statistical fluctuations. A systematic uncertainty of ∼0.3% for both R_{10}

Table 2 Summary of statistical and systematic uncertainties on the measurements of R_{10} and R_γ

	$\delta(R_{10}) \times 10^5$	$\delta(R_\gamma) \times 10^5$
Statistical error	0.024	0.066
Systematic error		
Counting:		
fit	0.007	0.004
DE	0.005	–
Efficiency:		
kin	0.014	0.009
trigger	0.009	0.006
e, μ cluster	0.005	0.003
γ cluster	–	0.003
Total systematic error	0.019	0.013

and $\mathrm{d}R_\gamma/\mathrm{d}E_\gamma$, independently on E_γ, is derived by scaling the uncorrelated errors so that the reduced χ^2 value equals unity (see also Table 2).

K_{e2} event counting is also affected by the uncertainty on f_{DE}, the fraction of K_{e2} events in the fit region which are due to DE process. This error has been evaluated by repeating the measurement of R_{10} with values of f_{DE} varied within its uncertainty, which is ~4% according to our measurement of the $K_{e2\gamma}$ differential spectrum (Sects. 3.1 and 6). Since the m_ℓ^2 distributions for $K_{e2\gamma}$ with $E_\gamma < 10$ MeV and with $E_\gamma > 10$ MeV overlap only partially, the associated fractional variation on R_{10} is reduced: the final error due to DE uncertainty is 0.2% (Table 2).

Different contributions to the systematic uncertainty on $\epsilon_{e2}/\epsilon_{\mu 2}$ are listed in Table 2. These errors are dominated by the statistics of the control samples used to correct the MC evaluations. In addition, we studied the variation of each correction with modified control-sample selection criteria. We found neglible contributions in all cases but for the kink and quality cuts corrections, for which the bias due to the control-sample selection and the statistics contribute at the same level.

The total systematic error is ~0.8% for both R_{10} and R_γ measurements, to be compared with statistical accuracies, which are 1% and 4.5%, respectively. As a further cross-check on the results, and particularly on the criteria adopted to obtain the data/MC corrections, we measured with the same analysis method the ratio $R_{\ell 3} = \Gamma(K_{e3})/\Gamma(K_{\mu 3})$. We found $R_{\ell 3} = 1.507 \pm 0.005_{\mathrm{stat}}$ and $R_{\ell 3} = 1.510 \pm 0.006_{\mathrm{stat}}$ for K^+ and K^-. These results agree within the quoted accuracy with the value expected from the world-average form-factor slope measurements [17], $R_{\ell 3} = 1.506 \pm 0.003$.

6 Results and interpretation

6.1 R_K and lepton-flavor violation

The number of $K \to e\nu(\gamma)$ events with $E_\gamma < 10$ MeV, the number of $K \to \mu\nu(\gamma)$ events, the ratio of K_{e2} to $K_{\mu 2}$ efficiencies and the measurement of R_{10} are given in Table 3 for K^+, K^- and both charges combined. K^+ and K^- results are consistent within the statistical error. The systematic uncertainty is common to both charges.

To compare the R_{10} measurement with the inclusive R_K prediction from SM, we take into account the acceptance of the 10 MeV cut for IB, (5). We obtain:

$$R_K = (2.493 \pm 0.025_{\mathrm{stat}} \pm 0.019_{\mathrm{syst}}) \times 10^{-5}, \tag{8}$$

in agreement with the SM prediction of (1). In the framework of MSSM with lepton-flavor violating (LFV) couplings, R_K can be used to set constraints in the space of relevant parameters, using the following expression [4]:

$$R_K = R_K^{\mathrm{SM}} \times \left[1 + \left(\frac{m_K^4}{m_H^4}\right)\left(\frac{m_\tau^2}{m_e^2}\right)|\Delta_R^{31}|^2 \tan^6\beta\right], \tag{9}$$

where M_H is the charged-Higgs mass, Δ_R^{31} is the effective e-τ coupling constant depending on MSSM parameters, and $\tan\beta$ is the ratio of the two Higgs superfields vacuum expectation values. The regions excluded at 95% C.L. in the plane M_H–$\tan\beta$ are shown in Fig. 10 for different values of the effective LFV coupling Δ_R^{31}.

6.2 Measurement of $\mathrm{d}R_\gamma/\mathrm{d}E_\gamma$

Results on the differential spectrum for $p_e > 200$ MeV are given in Table 4. For each E_γ bin we measure ΔR_γ, the integral of $\mathrm{d}R_\gamma/\mathrm{d}E_\gamma$ over the bin width. In Fig. 11 top, our measurements are compared to the prediction from χPT at $\mathcal{O}(p^4)$ [5] and from the Light Front Quark model (LFQ)

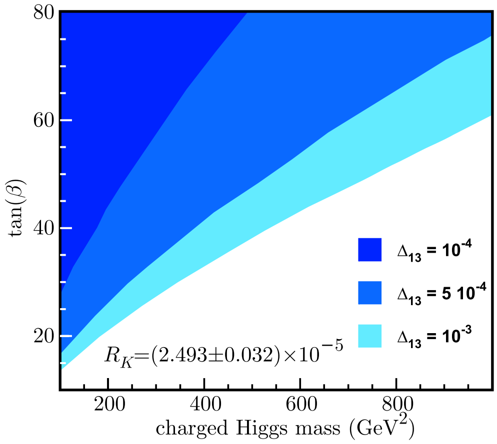

Fig. 10 Excluded regions at 95% C.L. in the plane M_H–$\tan\beta$ for $\Delta_R^{31} = 10^{-4}, 5 \times 10^{-3}, 10^{-3}$

Table 3 Number of K_{e2} and $K_{\mu 2}$ events, efficiency ratios and results for R_{10} for K^+, K^-, and both charges combined; first error is statistical, second one is systematic.

	N(K_{e2})	N($K_{\mu 2}$)	$\epsilon_{e2}/\epsilon_{\mu 2}$	R_{10}
K^+	$6348 \pm 92 \pm 23$	2.878×10^8	$0.944 \pm 0.003 \pm 0.007$	$(2.336 \pm 0.033 \pm 0.019) \times 10^{-5}$
K^-	$6064 \pm 91 \pm 22$	2.742×10^8	$0.949 \pm 0.002 \pm 0.007$	$(2.330 \pm 0.035 \pm 0.019) \times 10^{-5}$
$K^\pm$	$12412 \pm 129 \pm 45$	5.620×10^8	$0.947 \pm 0.002 \pm 0.007$	$(2.333 \pm 0.024 \pm 0.019) \times 10^{-5}$

Table 4 $\mathrm{d}R_\gamma/\mathrm{d}E_\gamma$ results. Most of the efficiency ratio error is common to all energy bins

E_γ (MeV)	$\epsilon(e2)/\epsilon(\mu 2)$	ΔR_γ (10^{-6})
10 to 50	0.104 ± 0.003	$0.94 \pm 0.30 \pm 0.03$
50 to 100	0.192 ± 0.001	$2.03 \pm 0.22 \pm 0.02$
100 to 150	0.184 ± 0.001	$4.47 \pm 0.30 \pm 0.03$
150 to 200	0.183 ± 0.001	$4.81 \pm 0.37 \pm 0.04$
200 to 250	0.174 ± 0.002	$2.58 \pm 0.26 \pm 0.03$

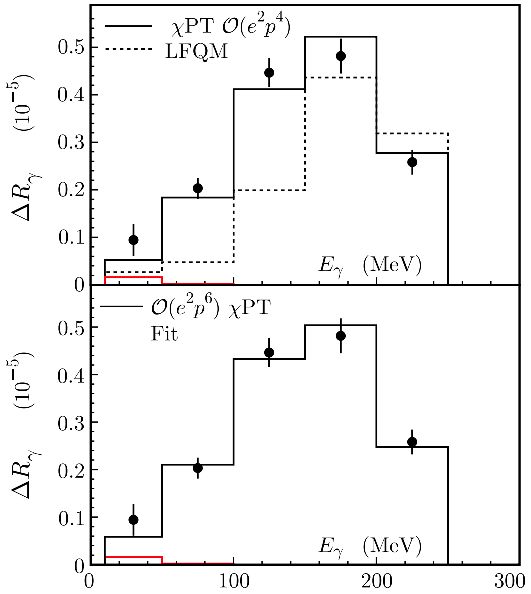

Fig. 11 (Color online) $\Delta R_\gamma = [1/\Gamma(K_{\mu 2})] \times [\mathrm{d}\Gamma(K_{e2\gamma}/\mathrm{d}E_\gamma]$ vs. E_γ. On *top* data (*black dots*) are compared to χPT predictions at $\mathcal{O}(e^2p^4)$ and to the LFQ model, see text. At the *bottom* data are fitted to χPT at $\mathcal{O}(e^2p^6)$. The IB contribution is shown (*red line*)

of [18]. Integrating over E_γ from 10 MeV to 250 MeV, we obtain:

$$R_\gamma = (1.483 \pm 0.066_{\text{stat}} \pm 0.013_{\text{syst}}) \times 10^{-5}, \tag{10}$$

in agreement with the prediction $R_\gamma = 1.447 \times 10^{-5}$, which is obtained using the values for the effective couplings (V and A) from $\mathcal{O}(e^2p^4)$ χPT [5] and using world-average values for all of the other relevant parameters. The R_γ prediction includes a 1.32(1)% contribution from IB. This result confirms within a 4% error the amount of DE component in our MC.

The comparison of the measured spectrum with the χPT prediction shown in Fig. 11 top suggests the presence of a form factor, giving a dependence of the effective couplings on the transferred momentum, $W^2 = M_K^2(1-x)$, as predicted by χPT at $\mathcal{O}(e^2p^6)$ [18]. The form-factor parameters are obtained by fitting the measured E_γ distribution with the theoretical differential decay width given in (2), with the vector effective coupling expanded at first order in x: $V = V_0(1+\lambda(1-x))$. The axial effective coupling A is assumed to be independent on W as predicted by χPT at $\mathcal{O}(e^2p^6)$ [18]. The small contribution from DE$^-$ transition to our selected events does not allow a fit to the related $V-A$ component. Therefore, in the fit $V_0 - A$ is kept fixed at the expectation from χPT at $O(e^2p^4)$, while $V_0 + A$ and λ are the free parameters. The result of this fit is shown in Fig. 11 bottom. We obtain:

$$V_0 + A = 0.125 \pm 0.007_{\text{stat}} \pm 0.001_{\text{syst}},$$

$$\lambda = 0.38 \pm 0.20_{\text{stat}} \pm 0.02_{\text{syst}},$$

with a correlation of -0.93 and a $\chi^2/\text{ndof} = 1.97/3$. Our fit confirms at $\sim 2\sigma$ the presence of a slope in the vector form factor, in agreement with the value from χPT at $O(e^2p^6)$, $\lambda \sim 0.4$.

7 Conclusions

We have performed a comprehensive study of the process $K_{e2\gamma}$. We have measured the ratio of $K_{e2\gamma}$ and $K_{\mu 2}$ widths for photon energies smaller than 10 MeV, without photon detection requirement. We find:

$$R_{10} = (2.333 \pm 0.024_{\text{stat}} \pm 0.019_{\text{stat}}) \times 10^{-5}. \tag{11}$$

From this result we derive the inclusive ratio R_K to be compared with the SM prediction:

$$R_K = (2.493 \pm 0.025_{\text{stat}} \pm 0.019_{\text{syst}}) \times 10^{-5}, \tag{12}$$

in excellent agreement with the SM prediction

$$R_K = (2.477 \pm 0.001) \times 10^{-5}. \tag{13}$$

Our result improves the accuracy with which R_K is known by a factor of 5 with respect to the present world average and allows constraints to be set on new physics contributions in the MSSM with lepton flavor violating couplings as shown in Fig. 10.

To obtain the value of R_K from the measurement of R_{10} knowledge of radiative effects is required for both inner bremsstrahlung and direct emission. The latter is important for the helicity suppressed $K \to e\nu$ decay but is not precisely known nor the differential width has ever been measured. We have therefore measured the differential decay width for $K_{e2\gamma}$ as a function of E_γ, normalized to $K_{\mu 2}$, in the momentum region $p_e > 200$ MeV, in the kaon rest frame. Our result for the direct emission width is in agreement with the expectation from χPT and gives an indication of the presence of $\mathcal{O}(e^2p^6)$ contributions.

Acknowledgements We warmly thank M. Testa for her help in producing the control samples used throughout the analysis. We thank the DAΦNE team for their efforts in maintaining low background running conditions and their collaboration during all data-taking. We want to thank our technical staff: G.F. Fortugno and F. Sborzacchi for their dedicated work to ensure an efficient operation of the KLOE Computing Center; M. Anelli for his continuous support to the gas system and the safety of the detector; A. Balla, M. Gatta, G. Corradi and G. Papalino for the maintenance of the electronics; M. Santoni, G. Paoluzzi and R. Rosellini for the general support to the detector; C. Piscitelli for his help during major maintenance periods. This work was supported in part by EURODAPHNE, contract FMRX-CT98-0169; by the German Federal Ministry of Education and Research (BMBF) contract 06-KA-957; by the German Research Foundation (DFG), 'Emmy Noether Programme', contracts DE839/1-4.

References

1. W.J. Marciano, A. Sirlin, Phys. Rev. Lett. **71**, 3629 (1993)
2. M. Finkemeier, Phys. Lett. B **387**, 391 (1996)
3. V. Cirigliano, I. Rosell, Phys. Rev. Lett. **99**, 231801 (2007)
4. A. Masiero, P. Paradisi, R. Petronzio, J. High Energy Phys. **0811**, 042 (2008)
5. J. Bijnens, G. Colangelo, G. Ecker, J. Gasser, arXiv:hep-ph/9411311. Published in 2nd DAPHNE Physics Handbook:315–389
6. J. Heintze et al., Nucl. Phys. B **149**, 365 (1979)
7. N. Cabibbo, Phys. Rev. Lett. **10**, 531 (1963)
8. M. Adinolfi et al. (KLOE Coll.), Nucl. Instrum. Methods A **488**, 51 (2002)
9. M. Adinolfi et al. (KLOE Coll.), Nucl. Instrum. Methods A **482**, 364 (2002)
10. M. Adinolfi et al. (KLOE Coll.), Nucl. Instrum. Methods A **492**, 134 (2002)
11. F. Ambrosino et al. (KLOE Coll.), Nucl. Instrum. Methods A **534**, 403 (2004)
12. C. Gatti, Eur. Phys. J. C **45**, 417 (2006)
13. F. Ambrosino et al. (KLOE Coll.), J. High Energy Phys. **02**, 098 (2008)
14. F. Ambrosino et al. (KLOE Coll.), Phys. Lett. B **632**, 4350 (2006)
15. F. Ambrosino et al. (KLOE Coll.), Phys. Lett. B **636**, 166 (2006)
16. F. Ambrosino et al. (KLOE Coll.), J. High Energy Phys. **12**, 105 (2007)
17. M. Antonelli et al., arXiv:0801.1817 [hep-ph]
18. C.H. Chen, C.Q. Geng, C.C. Lih, Phys. Rev. D **77**, 014004 (2008)